nature communications

Article

https://doi.org/10.1038/s41467-024-48815-y

Self acceleration from spectral geometry in dissipative quantum-walk dynamics

Received: 2 October 2023

Accepted: 10 May 2024

Published online: 23 May 2024

Check for updates

Peng Xue[1] ✉, Quan Lin[1], Kunkun Wang[2], Lei Xiao[1], Stefano Longhi[3,4] ✉ & Wei Yi[5,6] ✉

The dynamic behavior of a physical system often originates from its spectral properties. In open systems, where the effective non-Hermitian description enables a wealth of spectral structures in the complex plane, the concomitant dynamics are significantly enriched, whereas the identification and comprehension of the underlying connections are challenging. Here we experimentally demonstrate the correspondence between the transient self-acceleration of local excitations and the non-Hermitian spectral topology using lossy photonic quantum walks. Focusing first on one-dimensional quantum walks, we show that the measured short-time acceleration of the wave function is proportional to the area enclosed by the eigenspectrum. We then reveal a similar correspondence in two-dimension quantum walks, where the self-acceleration is proportional to the volume enclosed by the eigenspectrum in the complex parameter space. In both dimensions, the transient self-acceleration crosses over to a long-time behavior dominated by a constant flow at the drift velocity. Our results unveil the universal correspondence between spectral topology and transient dynamics, and offer a sensitive probe for phenomena in non-Hermitian systems that originate from spectral geometry.

In both classical and quantum mechanics, the dynamics of a system are intimately connected with its spectral features through the equations of motion[1–4]. Just as the energy of a celestial body impacts its trajectory[5], the energy quantization accounts for the spontaneous collapse and revival in quantum models[2]. In solid materials, transport of electrons depends on the lattice dispersion[6–8], with strict connections between spectral and dynamical features of transport. For example, in a clean lattice with absolutely continuous spectrum, transport is ballistic, while in disordered lattices, the different nature of the energy spectrum greatly impacts the spreading dynamics of the wave function, leading to distinct behaviors ranging from the Anderson localization to diffusive and intermittent quantum dynamics[9]. These examples, however, all concern isolated systems with completely real energy spectra. For open systems that exchange energy or particles with its environment, an effective non-Hermitian description is often adopted, where the underpinning non-Hermitian Hamiltonians feature complex eigenspectra[10–12]. This enables a rich variety of spectral geometries in the complex plane, with non-trivial consequences on the system behavior[13–21]. The dynamics generated by non-Hermitian Hamiltonians are often less intuitive than those of conventional Hermitian systems. For example, the semiclassical equations of non-Hermitian Hamiltonians generalize the Ehrenfest theorem in a nontrivial way[22], leading to phase-space dynamics with a changing metric structure[22–24]. Beyond the semiclassical models, recent studies of non-Hermitian Hamiltonians with the non-Hermitian skin effect[17,25] unravelled that, spectral features such as the closing of

[1]School of Physics, Southeast University, Nanjing 211189, China. [2]School of Physics and Optoelectronic Engineering, Anhui University, Hefei 230601, China. [3]Dipartimento di Fisica, Politecnico di Milano, Piazza L. da Vinci 32, Milano I-20133, Italy. [4]IFISC (UIB-CSIC) Instituto de Fisica Interdisciplinar y Sistemas Complejos, Palma de Mallorca E-07122, Spain. [5]CAS Key Laboratory of Quantum Information, University of Science and Technology of China, Hefei 230026, China. [6]CAS Center For Excellence in Quantum Information and Quantum Physics, Hefei 230026, China. ✉e-mail: gnep.eux@gmail.com; stefano.longhi@polimi.it; wyiz@ustc.edu.cn

the imaginary gap on the complex plane[25–32], or the overall spectral topology[33–41], can have detectable dynamic consequences, including anomalous relaxation dynamics[42–44], boundary accumulations of loss in the dynamics (known as the edge burst)[30–32], and the persistent directional flow which has served as an experimental signature for the non-Hermitian skin effect[18,19,45–55]. However, as most of such dynamic behaviors only dominate at long times and require post selection to avoid quantum jumps, their experimental identification in genuinely quantum systems may be challenging.

In this work, we experimentally reveal the impact of non-Hermitian spectral topology in transient dynamics, by studying the propagation of a local excitation along a dissipative lattice using photonic quantum walks. We show that the short-time, center-of-mass acceleration of the wave function, dubbed self-acceleration[56] because of the absence of any external force, is proportional to the area enclosed by the eigenenergy spectrum of the system on the complex plane. While the direction of the propagation is given by the spectral winding number, the self-acceleration vanishes at long times, giving way to a directional flow with a constant drift velocity. The correspondence between the spectral geometry and bulk dynamics also persists in a wide class of two-dimensional systems, for which we demonstrate that the self-acceleration becomes proportional to the volume enclosed by the eigenspectrum in the complex parameter space. Our experiment establishes a fundamental correspondence between the spectral geometry and short-time dynamics in non-Hermitian systems, complementing existing experiments on the long-time dynamics and chiral amplification. As the spectral topology is intimately connected with the non-Hermtian skin effect, self-acceleration offers a practical and sensitive dynamic signal for its detection, particularly in quantum systems where decoherence dominates at long times.

Results

Time-multiplexed quantum walk

We simulate the dynamics of a local excitation along a dissipative lattice using photonic quantum walks[57–59] (see "Methods" and the Supplementary Information Note 1). Taking the more general two-dimensional quantum walk as an example, we implement the non-unitary Floquet operator

$$U = M_y S_y R(\theta_2) M_x S_x R(\theta_1), \tag{1}$$

where shift operators are defined as $S_j = \sum_{\boldsymbol{r}} |0\rangle\langle 0| \otimes |\boldsymbol{r} - \boldsymbol{e}_j\rangle\langle \boldsymbol{r}| + |1\rangle\langle 1| \otimes |\boldsymbol{r} + \boldsymbol{e}_j\rangle\langle \boldsymbol{r}|$ with $\boldsymbol{r} = (x,y) \in \mathbb{Z}^2$ labeling the coordinates of the lattice sites, $j \in \{x,y\}$, and $\boldsymbol{e}_x = (1,0)$ and $\boldsymbol{e}_y = (0,1)$. The shift operators move the walker in the corresponding directions, depending on the walker's internal degrees of freedom in the basis of $\{|0\rangle,|1\rangle\}$ (dubbed the coin states). The coin operator acts in the subspace of coin states $R(\theta_{1,2}) = \begin{pmatrix} \cos\theta_{1,2} & i\sin\theta_{1,2} \\ i\sin\theta_{1,2} & \cos\theta_{1,2} \end{pmatrix} \otimes \mathbb{1}_{\boldsymbol{r}}$, where $\mathbb{1}_{\boldsymbol{r}} = \sum_{\boldsymbol{r}} |\boldsymbol{r}\rangle\langle \boldsymbol{r}|$. The gain-loss operators are given by $M_j = \begin{pmatrix} e^{\gamma_j} & 0 \\ 0 & e^{-\gamma_j} \end{pmatrix} \otimes \mathbb{1}_{\boldsymbol{r}}$, which make the quantum walk non-unitary for finite γ_x or γ_y. For the momentum-space Hamiltonian corresponding to U, see the Supplementary Information Note 1.

In the experiment, we encode the internal coin states $\{|0\rangle,|1\rangle\}$ in the photon polarizations $\{|H\rangle,|V\rangle\}$, and the external spatial modes through the discretized temporal shifts. For the latter, we build path-dependent time delays into the loop, so that the spatial superposition of the photonic walker is translated to the temporal superposition of multiple well-resolved pulses within each discrete time step[60]. To encode spatial modes in two dimensions, the temporal modes are further separated into two different time scales by the free-space Mach–Zehnder interferometer: 80 ns in the x-dimension and 4.83 ns in the y-dimension. For detection, we record the arrival time of the photons using avalanche photodiodes with the help of an acousto-optical modulator serving as an optical switch to remove undesired pulses[61].

In the quantum-walk dynamics, the time-evolved state at the end of each discrete time step t is $|\psi(t)\rangle = U^t|\psi(0)\rangle = e^{-iHt}|\psi(0)\rangle$, where we define an effective Hamiltonian H. Apparently, the quantum walk implements a stroboscopic simulation of the Hamiltonian H at integer time steps (see the Supplementary Information Note 1). We measure the center-of-mass position of the walker, defined through[56]

$$\boldsymbol{n}_{CM}(t) = \frac{\sum_{\boldsymbol{r}} \langle\psi(t)|\boldsymbol{r}|\psi(t)\rangle}{\sum_{\boldsymbol{r}} \langle\psi(t)|\psi(t)\rangle}. \tag{2}$$

As illustrated in Fig. 1, starting from a local excitation, the motion of $\boldsymbol{n}_{CM} = (x_{CM}, y_{CM})$ is closely connected with the spectral geometry of the effective Hamiltonian H on the complex plane. More explicitly, transforming H to the momentum space, we have $H(\boldsymbol{k})|\psi_\pm(\boldsymbol{k})\rangle = E_\pm(\boldsymbol{k})|\psi_\pm(\boldsymbol{k})\rangle$, where $\boldsymbol{k}$ belongs to the first Brillouin zone, and $E_\pm(\boldsymbol{k})$ and $|\psi_\pm(\boldsymbol{k})\rangle$ are respectively the eigenenergies and eigenstates under the periodic boundary condition (PBC), with the subscripts $\pm$ indicating the band index. For a local initial state that is an equal-weight superposition of all eigenstates within a given band, for instance, $|\psi(0)\rangle = \sum_{\boldsymbol{k}} |\psi_+(\boldsymbol{k})\rangle \otimes |\boldsymbol{k}\rangle$, the short-time behavior of $\boldsymbol{n}_{CM}$ reads (see "Methods")

$$x_{CM}(t) \simeq \frac{1}{2} a_x t^2 - \frac{1}{2}, \quad y_{CM}(t) \simeq \frac{1}{2} a_y t^2 + \frac{1}{2}, \tag{3}$$

where

$$\begin{aligned} a_x &= \frac{1}{\pi^2}\int_{-\pi}^{\pi} \mathrm{d}k_x \mathrm{d}k_y E_I \frac{\partial E_R}{\partial k_x} = \frac{2}{\pi}\int_{-\pi}^{\pi} \mathrm{d}\,k_y \mathcal{A}_x(k_y), \\ a_y &= \frac{1}{\pi^2}\int_{-\pi}^{\pi} \mathrm{d}k_x \mathrm{d}k_y E_I \frac{\partial E_R}{\partial k_y} = \frac{2}{\pi}\int_{-\pi}^{\pi} \mathrm{d}\,k_x \mathcal{A}_y(k_x). \end{aligned} \tag{4}$$

Here E_R and E_I are, respectively, the real and imaginary components of E_+. Importantly, a_x and a_y suggest that the short-time self-acceleration rate is proportional to the volume enclosed by the eigenspectrum of the corresponding band in the complex parameter space. An alternative understanding is that the self-acceleration rate is proportional to the averaged area enclosed by $E_+(k_x,k_y)$ on the complex plane as k_y traverses the Brillouin zone, as shown in Fig. 1. It should be mentioned that, in non-Hermitian systems, self-acceleration of the wave function in the absence of external forces is a universal phenomenon observed for rather arbitrary excitations that are initially localized (see "Methods"). However, it is only when the system is initially prepared in an equal-weight superposition of all eigenstates within a given band, that the ensuing self-acceleration relates to the spectral geometry through a_x and a_y.

Simulating the one-dimensional dynamics

For our experimental demonstration, we first consider the case of one-dimensional quantum walks. In one-dimensional lattices, a general correspondence can be established between spectral geometry and self-acceleration. Such a correspondence is grounded on a general theorem given in the Supplementary Information Note 2, which extends previous theoretical results[56]. Basically, for suitable initial preparation of the system, the self-acceleration rate is proportional to the area enclosed by the PBC eigenspectrum of a given lattice band on the complex plane. Based on the general two-dimensional setup in Fig. 1, one-dimensional quantum walks can be realized by simply removing the free-space Mach–Zehnder interferometer within the

https://doi.org/10.1038/s41467-024-48815-y

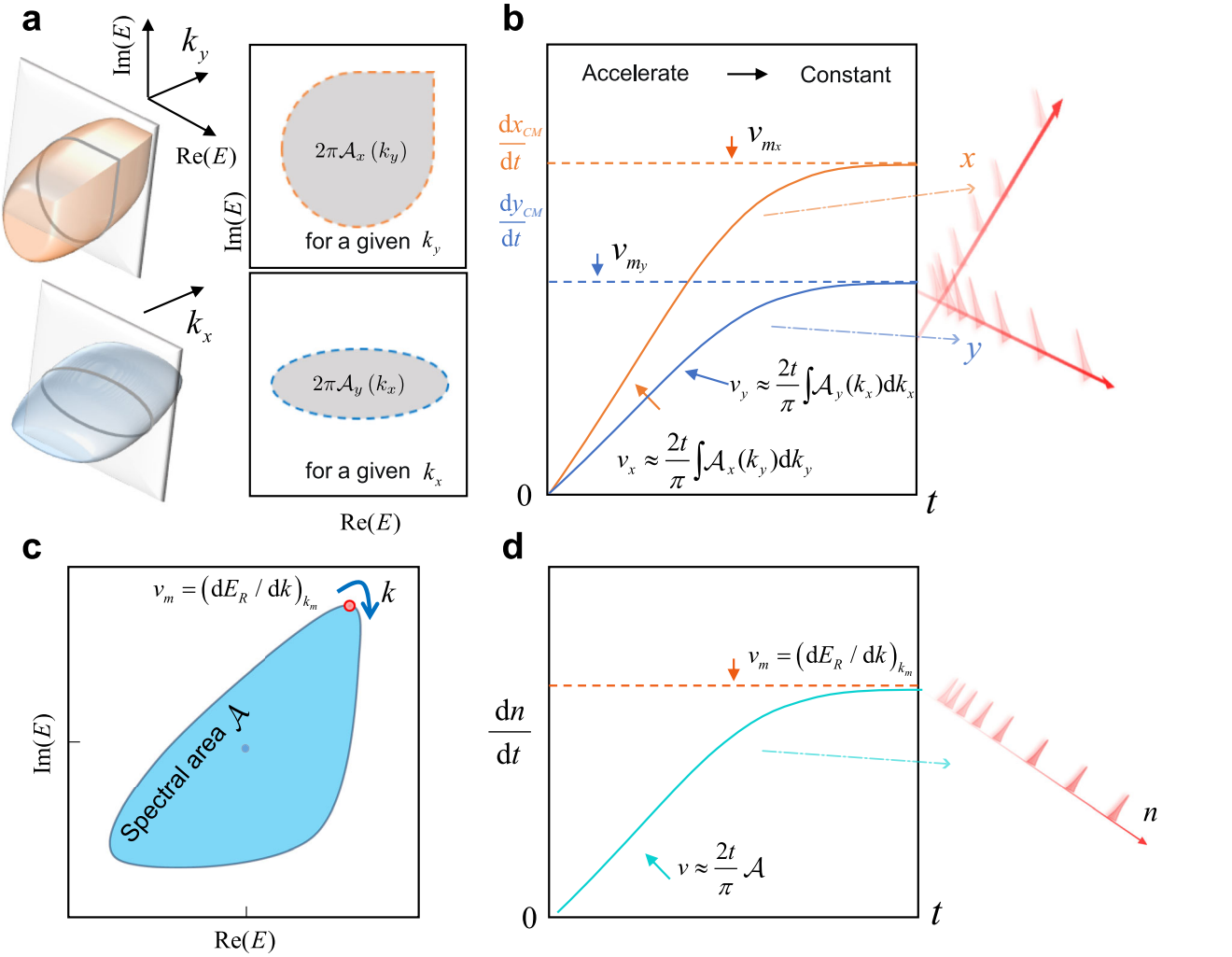

Fig. 1 | Illustration of the connection between self-acceleration and spectral geometry. a A schematic of the PBC energy spectra in a two-dimensional system with k_y (upper panel) and k_x (lower panel) as a parameter. **b** The corresponding two different volumes lead to distinct dynamic behaviors, i.e., different accelerated speeds of the motion of the wave packets in two directions, and eventually approach to a constant. **c** A schematic with a finite energy spectrum area in a one-dimensional system. **d** The motion of the wave packet shifts from accelerated to constant velocity as time increases.

loop. The resulting Floquet operator is given by

$$U = S_x M_x R(\theta). \tag{5}$$

We focus on the parameter regime with θ being quite close to $\pi/2$ (we choose $\theta = 0.45\pi$ for experiment), where the complex eigenenergies of the effective Hamiltonian H are approximately (see "Methods")

$$E_\pm(k) \approx \pm\frac{\pi}{2} \mp \cos\theta\cos(k - i\gamma_x), \tag{6}$$

the last term of Eq. (6) corresponding to those of a typical Hatano–Nelson model, i.e., $H_{HN} = (1/2)\cos(\theta)e^{ik-\gamma_x} + (1/2)\cos(\theta)e^{-ik+\gamma_x}$. We initialize the system in the superposition state (representing a local excitation) $|\psi(0)\rangle_1 = e^{\gamma_x}|0\rangle \otimes |x = -1\rangle + |1\rangle \otimes |x = 0\rangle$, which is an equal-weight superposition of the Bloch states (in the first Brillouin zone) of H with eigenenergy $E_+(k)$. The experimental implementation of such a local initial state, which is pivotal to our measurement scheme, is discussed in "Methods" and the Supplementary Information Note 3. The resulting short-time dynamics of x_{CM} then follows that in Eq. (3), with the self-acceleration rate given by

$$a_x = \frac{2}{\pi}\int_{-\pi}^{\pi} dk_x E_I \frac{d}{dk} E_R := \frac{2}{\pi}\mathcal{A}. \tag{7}$$

Here $\mathcal{A}$ corresponds to the area enclosed by the complex eigenenergy $E_+(k_x)$ in the complex plane, taken with the appropriate sign depending on the circulation direction of the PBC energy loop. Such a sign naturally indicates the direction of self-acceleration.

In Fig. 2a–c, we show the measured spatial population evolution of the dynamics under different gain-loss parameters γ_x. The wave-function propagation becomes asymmetric when the gain-loss parameter γ_x becomes finite. In Fig. 2d–f, we show the measured $x_{CM}(t)$, which are quadratic in time when $\gamma_x \neq 0$, consistent with the-oretical predictions. By fitting the center-of-mass propagation of the wave functions, we extract the quantity $\mathcal{A}$ from the self-acceleration rate (see Fig. 2g), which agrees well with the numerically calculated area enclosed by the eigenspectum $E_+(k)$ on the complex plane (see Fig. 2h). The self-acceleration in the one-dimensional model is a clear signature of the non-Hermitian skin effect under the open-boundary condition. In fact, in systems that do not display the non-Hermitian skin effects, the PBC energy spectrum collapses to an open arc enclosing a vanishing area $\mathcal{A} = 0$, and thus acceleration vanishes according to Eq. (7).

Simulating the two-dimensional dynamics

In two dimensions, we focus on the coin parameters close to $(\theta_1 = 0, \theta_2 = \pi/2)$, where the eigenenergies of the effective Hamiltonians

https://doi.org/10.1038/s41467-024-48815-y

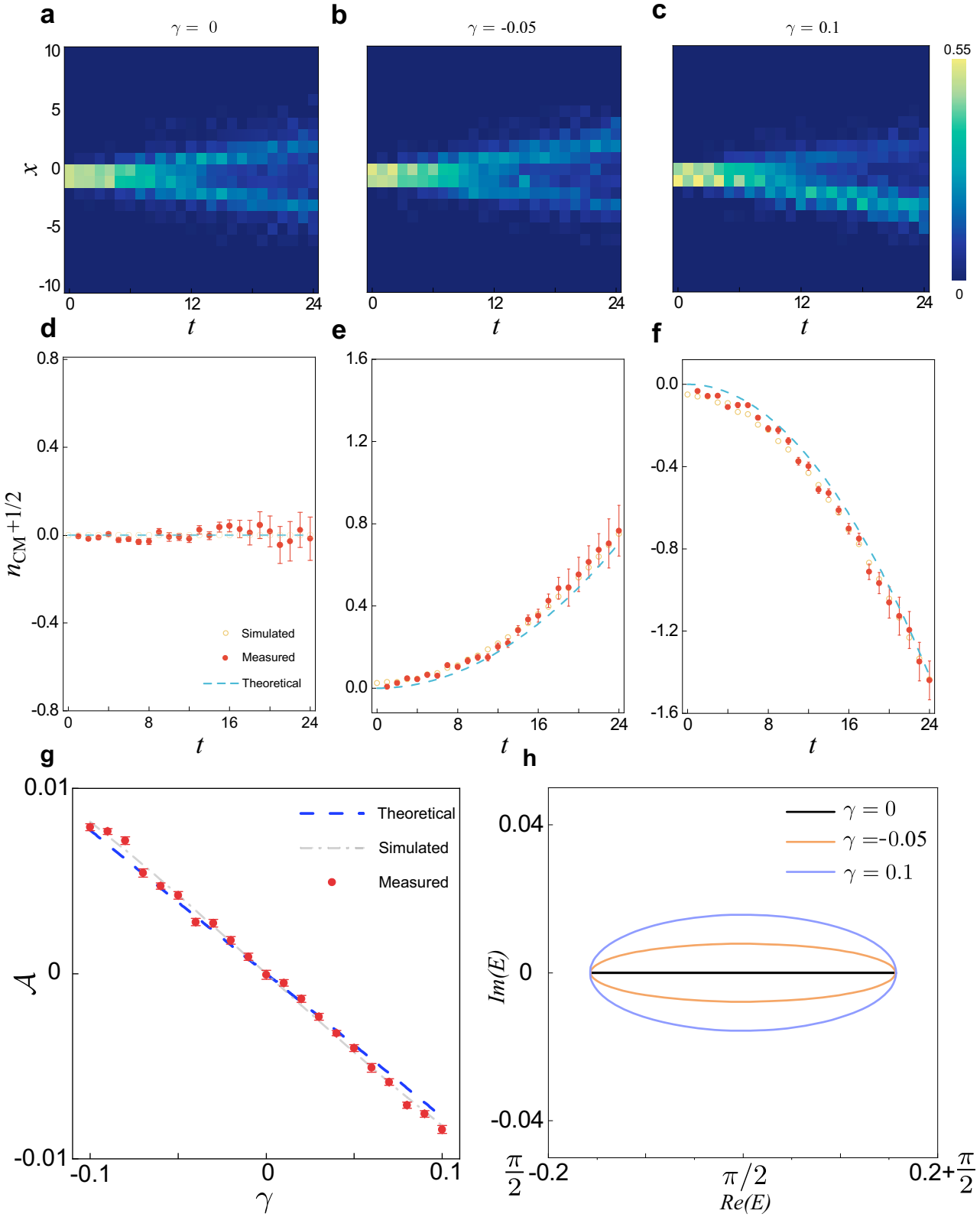

Fig. 2 | Self-acceleration in one-dimensional dynamics. a–c Dynamic evolutions governed by the effective non-Hermitian Hamiltonian with parameters $\gamma_x = 0$, $\gamma_x = -0.05$ and $\gamma_x = 0.1$, respectively. **d–f** Evolution of the center of mass $n_{CM}(t)$ as a function of the discrete time step t corresponding to the dynamic evolutions in (**a–c**), respectively. **g** Areas enclosed by $E_+(k)$ versus the gain-loss parameter $\gamma = \gamma_x$. We take a local initial state $|\psi(0)\rangle_1$ and the coin parameter $\theta = 0.45\pi$. **h** PBC energy spectra for increasing values of γ.

https://doi.org/10.1038/s41467-024-48815-y

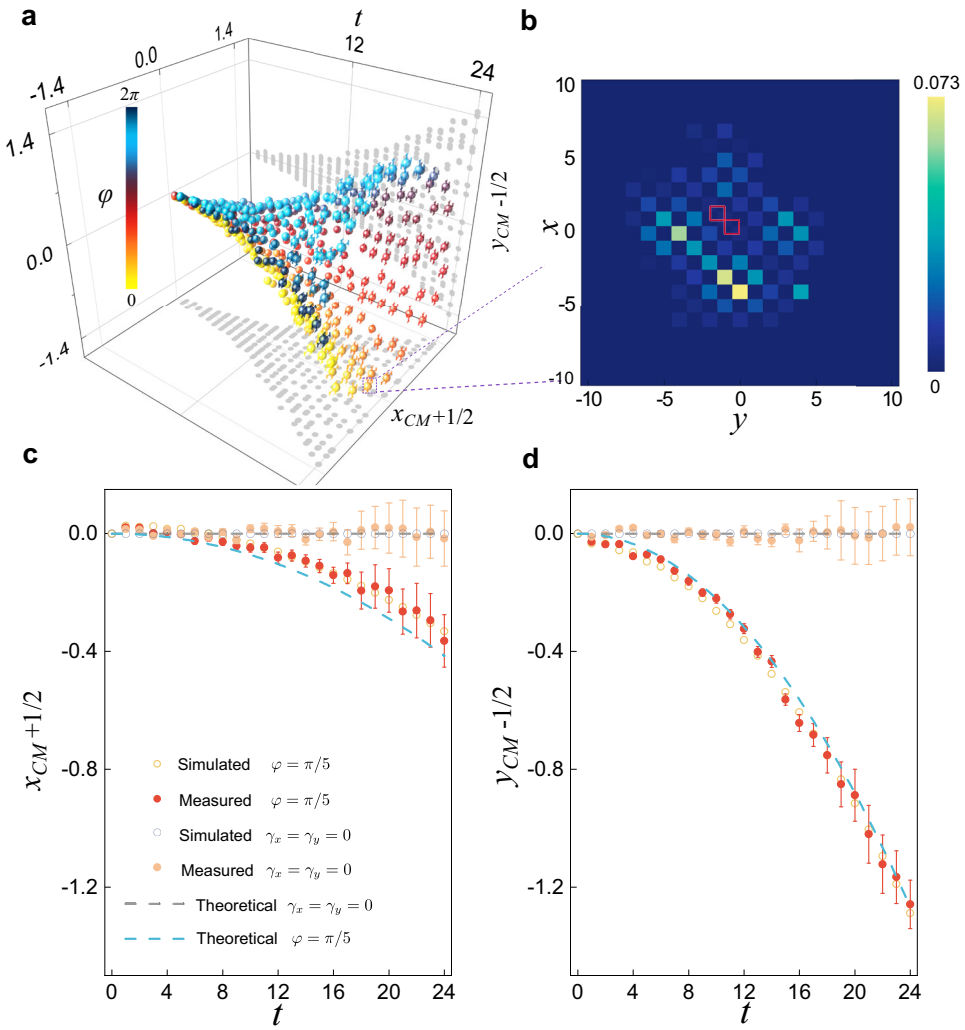

Fig. 3 | Self-acceleration in two-dimensional dynamics. a Wave packet center of mass $x_{CM}(t)$ ($y_{CM}(t)$) as a function of the discrete time step t. The gain-loss parameter is taken as $\gamma = 0.08$. **b** Probability distribution of the 24-time-step quantum walk with $\varphi = \pi/5$. We mark the position occupied by the initial state as the red square. **c**, **d** The wave packet center of mass $x_{CM}(t)$ ($y_{CM}(t)$) as a function of the discrete time step t with $\varphi = \pi/5$. The other parameters are $\theta_1 = 0.12$, $\theta_2 = \pi/2 - 0.12$, and the initial state $|\psi(0)\rangle_2$.

are

$$E_{\pm}(k_x,k_y) \approx \pm\tfrac{\pi}{2} \pm \tilde{E}(k_x,k_y). \tag{8}$$

Here $\tilde{E}(k_x,k_y) = \theta_1 \cos(k_y - i\gamma_y - k_x + i\gamma_x) - (\pi/2 - \theta_2)\cos(k_x - i\gamma_x + k_y - i\gamma_y)$ corresponds to single-band lattice on a two-dimensional square lattice, i.e., $\hat{H} = \sum_{n,m,k,l} H_{n,m,k,l}|n,m\rangle\langle k,l|$, with matrix Hamiltonian

$$\begin{aligned} H_{n,m,n-1,m+1} &= \theta_1 e^{(\gamma_y-\gamma_x)/2} \\ H_{n,m,n-1,m-1} &= (\theta_2 - \pi/2)e^{(-\gamma_y-\gamma_x)/2} \\ H_{n,m,n+1,m-1} &= \theta_1 e^{(\gamma_x-\gamma_y)/2} \\ H_{n,m,n+1,m+1} &= (\theta_2 - \pi/2)e^{(\gamma_y+\gamma_x)/2}, \end{aligned} \tag{9}$$

corresponding to the hopping amplitudes in four different directions.

We initialize the system in the local state $|\psi(0)\rangle_2 = |0\rangle \otimes |x=0,y=0\rangle - e^{\gamma_x-\gamma_y}|1\rangle \otimes |x=-1,y=1\rangle$, which is a superposition of all the Bloch states corresponding to $E_+(k_x,k_y)$, again facilitated by the choice of the coin parameters.

In Fig. 3a, we show the time evolution of (x_{CM}, y_{CM}) under different gain-loss parameters γ_x and γ_y, which are parameterized through $\gamma_x = \gamma\cos\varphi$ and $\gamma_y = \gamma\sin\varphi$. Consistent with a previous study[59], the tuning of the parameters gives rise to directional propagation in the two-dimensional plane (x- and y-direction), which underlies the emergence of the non-Hermitian skin effect when open boundaries are enforced. An example of the full population evolution is illustrated in Fig. 3b. Apparently, for finite γ_x or γ_y, the corresponding x_{CM} or y_{CM} exhibits quadratic behavior at early times, consistent with the predicted self-acceleration.

In Fig. 4, we explicitly demonstrate the correspondence between the spectral volume and the self-acceleration. For convenience, we focus on the case $\gamma_x = \gamma_y$, where the dynamics along the x and y directions are symmetric. Both the spectral volume and the fitted self-acceleration increase linearly with increasing $|\gamma_{x(y)}|$, consistent with the theoretical analysis. Similar to one-dimensional quantum walks, the self-acceleration is a precursor of persistent drift (or current) at long times and thus indicates the accumulation of excitation at the edges or corners of a finite two-dimensional domain (or equivalently, the appearance of the so-called non-reciprocal skin effect[16]). It should be mentioned that, in two-dimensional systems, the skin effect is a universal phenomenon that appears under rather arbitrary boundary shapes[16], and thus it persists even when the self-acceleration vanishes (see "Methods").

https://doi.org/10.1038/s41467-024-48815-y

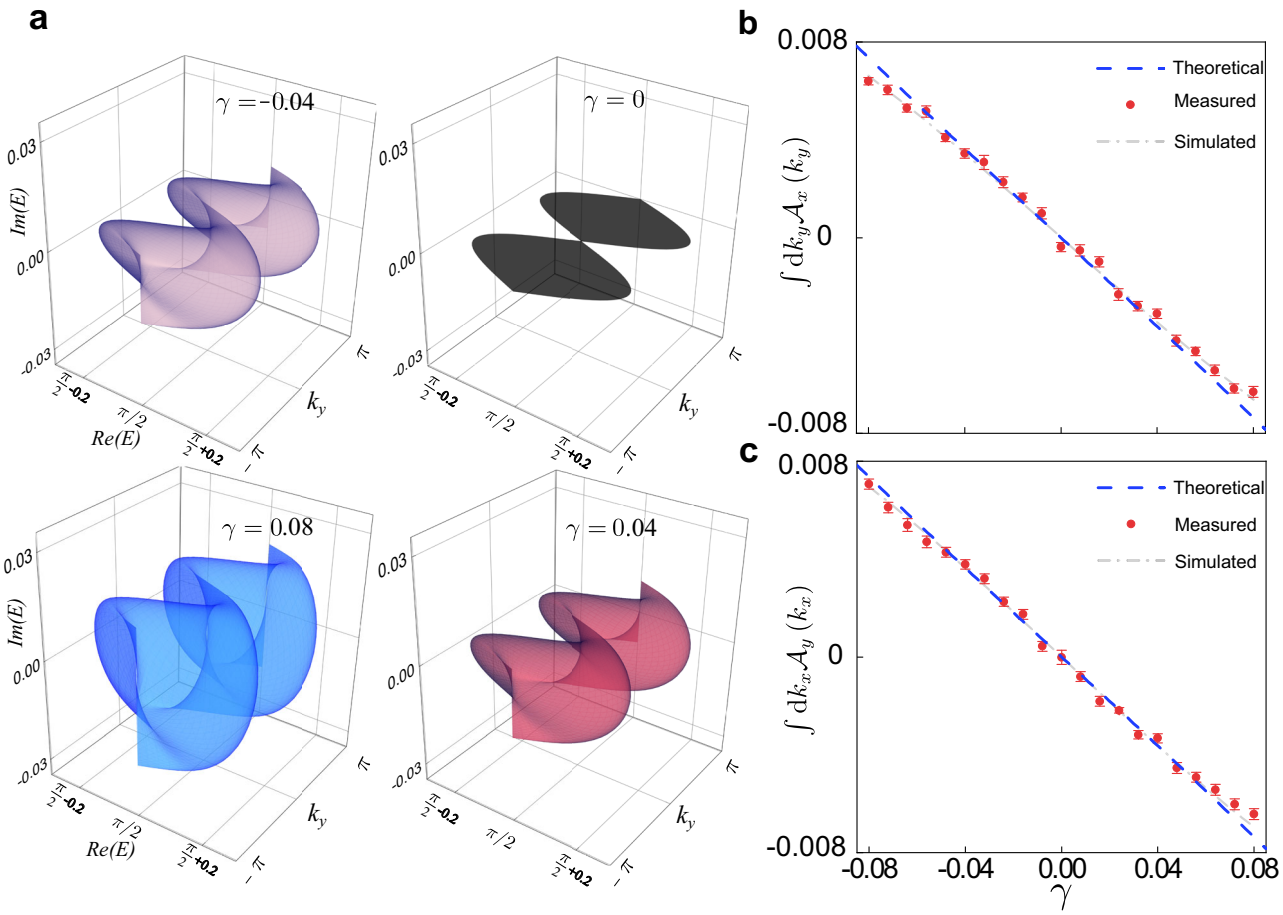

Fig. 4 | Measurement of the spectral volume. a PBC energy spectrum with k_y as a parameter and for $\gamma_x = \gamma_y$. The black, purple, red, and blue surfaces correspond to $\gamma_{x(y)} = 0$, $\gamma_{x(y)} = -0.04$, $\gamma_{x(y)} = 0.04$, and $\gamma_{x(y)} = 0.08$, respectively. **b**, **c** The average of the areas enclosed by $E_+(k_x,k_y)$ as a function of $\gamma_{x(y)}$. The other parameters are $\theta_1 = 0.12$, $\theta_2 = \pi/2 - 0.12$, and the initial state $|\psi(0)\rangle_2$. The blue dashed line represents the theoretical results, and the gray dashed lines correspond the results fitted by experimental data.

Crossover between short- and long-time dynamics

In the presence of a non-trivial spectral point-gap topology, it is well-established that the long-time dynamics of a local excitation is a directional propagation with a constant drift velocity[55,57,58], indicating that the self-acceleration ceases in the long-time evolution. The asymptotic drift velocities for two-dimensional dynamics are defined as the group velocity at the quasimomentum (k_{m_x},k_{m_y}), with

$$v_{m_{x,y}} = \frac{dE_R(k_{m_x},k_{m_y})}{d\,k_{x,y}} \tag{10}$$

where the eigenenergy $E_+(k_x = k_{mx}, k_y = k_{my})$ corresponds to the largest imaginary part of $E_+(k_x,k_y)$ (whose corresponding eigenmode survives at long times). As such, the combination of drift velocity at long times and self-acceleration at short times provides a complete correspondence between the spectral geometry and bulk dynamics of a local excitation.

In Fig. 5, we experimentally characterize the crossover from self-acceleration-dominated dynamics at short times (cyan dashed curves), to a flow at the drift velocity (purple dashed curves) at long times. This is achieved by choosing parameters such that the difference between self-acceleration and constant motion is appreciable at the experimentally accessible time steps.

Discussion

Unveiling the correspondence between dynamical and spectral properties of classical and quantum systems is a fundamental problem and a major challenge in different areas of physics. While such a correspondence is quite well understood in closed systems described by Hermitian Hamiltonians, it remains largely unexplored for open systems. Using dissipative photonic quantum walks, here we have experimentally demonstrated a fundamental correspondence between the spectral geometry and the dynamics of local excitations in open systems described by effective non-Hermitian Hamiltonians, showing that a non-trivial spectral topology generally corresponds to a transient self-acceleration of the wave function. Our results provide major advancements in the understanding of the correspondence between spectral geometry and dynamics beyond the Hermitian paradigm and could stimulate further studies on an emergent area of research.

Methods

Self-acceleration for one-dimensional quantum walks

In the one-dimensional quantum walk, the Floquet operator reads $U = S_x M_x R(\theta)$, where $S_x = \sum_x |0\rangle\langle 0| \otimes |x-1\rangle\langle x| + |1\rangle\langle 1| \otimes |x+1\rangle\langle x|$ is the spatial shift operator, $M_x = \sum_x \begin{pmatrix} e^{\gamma_x} & 0 \\ 0 & e^{-\gamma_x} \end{pmatrix} \otimes |x\rangle\langle x|$ is the gain-loss operator with the gain-loss parameter γ_x, and $R(\theta) = \sum_x \begin{pmatrix} \cos\theta & i\sin\theta \\ i\sin\theta & \cos\theta \end{pmatrix} \otimes |x\rangle\langle x|$ is the coin operator. In the momentum space, the Floquet operator U takes the form

$$U(k) = d_0\sigma_0 + id_x\sigma_x + id_y\sigma_y + id_z\sigma_z, \tag{11}$$

https://doi.org/10.1038/s41467-024-48815-y

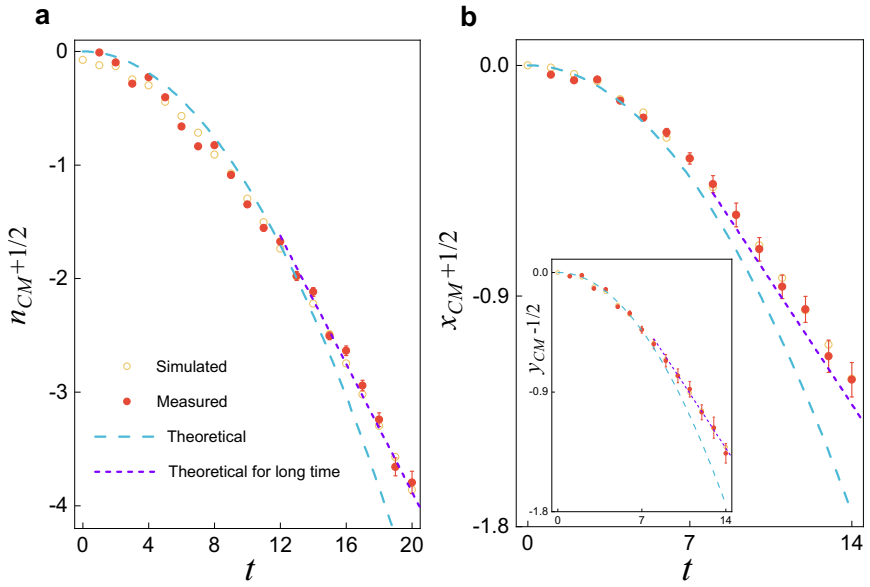

Fig. 5 | Connecting the short- and long-time dynamics. a Evolution of the center of mass $n_{CM}(t)$ as a function of the discrete-time step t in the one-dimensional quantum walks with $\theta = 0.41\pi$ and $\gamma_x = 0.15$. We take a local initial state $|\psi(0)\rangle_1$. **b** Wave packet center of mass $x_{CM}(t)$ ($y_{CM}(t)$) as a function of the discrete time step t in the two-dimensional quantum walks with $\gamma_x = \gamma_y = 0.26$, $\theta_1 = 0.12$, $\theta_2 = \pi/2 - 0.12$ the initial state $|\psi(0)\rangle_2$.

where the expressions for $d_{x,y,z}$ are given in the Supplementary Information Note 1, and $\sigma_{x,y,z}$ are the Pauli matrices. Defining the momentum-space Hamiltonian H_k through $U(k) = e^{-iH_k}$ (see the Supplementary Information Note 1), its quasienergies are given by

$$E_{\pm}(k) = \pm \arccos\left[\cos\theta\cos(k - i\gamma_x)\right], \tag{12}$$

with corresponding eigenstates (in the coin-state basis)

$$|\psi_{\pm}(k)\rangle = \begin{pmatrix} \frac{d_z \pm \sqrt{d_x^2 + d_y^2 + d_z^2}}{d_x + id_y} \\ 1 \end{pmatrix}. \tag{13}$$

In the experiment we set $\theta \approx \pi/2$, so that one has

$$\begin{aligned} E_{\pm}(k) &\simeq \pm\frac{\pi}{2} \mp \tilde{E}(k) \\ &= \pm\frac{\pi}{2} \mp \cos\theta\cos(k - i\gamma_x), \end{aligned} \tag{14}$$

and

$$|\psi_{\pm}(k)\rangle \simeq \begin{pmatrix} \pm e^{\gamma_x + ik} \\ 1 \end{pmatrix}. \tag{15}$$

Notice that $\tilde{E}(k)$ coincides with the dispersion of the Hatano–Nelson model with asymmetric nearest-neighbor hopping amplitudes $(1/2)\cos(\theta)e^{-\gamma_x}$ and $(1/2)\cos(\theta)e^{\gamma_x}$.

In our experiment, the quasi-local initial state can be expressed as

$$\begin{aligned} |\psi(0)\rangle_1 &= e^{\gamma_x}|0\rangle \otimes |x = -1\rangle + |1\rangle \otimes |x = 0\rangle \\ &= \frac{1}{2\pi}\int_{-\pi}^{\pi} \mathrm{d}\,k|\psi_+(k)\rangle \otimes |k\rangle. \end{aligned} \tag{16}$$

Note that the sum over k is approximated by integral at finite system size. The time-evolved state is then

$$|\psi(t)\rangle = \frac{(-i)^t}{2\pi}\int_{-\pi}^{\pi} \mathrm{d}\,k \begin{pmatrix} e^{\gamma_x + ik} \\ 1 \end{pmatrix} e^{i\tilde{E}(k)t} \otimes |k\rangle, \tag{17}$$

and the center-of-mass of the normalized wave function is defined through[56]

$$n_{\mathrm{CM}}(t) := \frac{\langle\psi(t)|x|\psi(t)\rangle}{\langle\psi(t)|\psi(t)\rangle}. \tag{18}$$

For short-time dynamics, making use of the truncated expansion $e^{2\tilde{E}_I(k)t} \approx 1 + 2\tilde{E}_I(k)t$, where $\tilde{E}(k) = \tilde{E}_R(k) + i\tilde{E}_I(k)$, after some straightforward calculations one obtains

$$n_{\mathrm{CM}}(t) = \frac{\mathcal{A}}{\pi}t^2 - \frac{1}{2}. \tag{19}$$

Here $\mathcal{A} := \int_{-\pi}^{\pi} \mathrm{d}k_x E_I \frac{\mathrm{d}}{\mathrm{d}k} E_R$ is the area enclosed by the complex quasienergy dispersion $E_+(k)$ in the complex plane.

In the long-time limit, the dynamics would be dominated by the Bloch mode k_m where $E_I(k)$ is the global maximum. This corresponds to the conditions $\left(\frac{\mathrm{d}E_I(k_m)}{\mathrm{d}k}\right) = 0$ and $\left(\frac{\mathrm{d}^2E_I(k_m)}{\mathrm{d}k^2}\right) < 0$. Defining $\xi = k - k_m$, we expand the quasienergy around k_m, where the leading orders give $E(k) \simeq E(k_m) + \left(\frac{\mathrm{d}E(k_m)}{\mathrm{d}k}\right)\xi + \frac{1}{2}\left(\frac{\mathrm{d}^2E(k_m)}{\mathrm{d}k^2}\right)\xi^2$. It follows that

$$\begin{aligned} n_{\mathrm{CM}}(t) &\approx \frac{2\pi t\left(\frac{\mathrm{d}E_R(k_m)}{\mathrm{d}k}\right)e^{2E_I(k_m)t}\int_{-\infty}^{\infty}\mathrm{d}\,\xi\, e^{t\xi^2\left(\frac{\mathrm{d}^2E_I(k_m)}{\mathrm{d}k^2}\right)}}{2\pi e^{2E_I(k_m)t}\int_{-\infty}^{\infty}\mathrm{d}\,\xi\, e^{t\xi^2\left(\frac{\mathrm{d}^2E_I(k_m)}{\mathrm{d}k^2}\right)}} \\ &= v_m t, \end{aligned} \tag{20}$$

where $v_m = \left(\frac{\mathrm{d}E_R(k_m)}{\mathrm{d}k}\right)$ is identified as the drift velocity.

Self-acceleration for two-dimensional quantum walks

Following a similar procedure outlined in the previous section, we derive the center-of-mass motion of the wave functions for two-dimensional quantum walks.

We start from the Floquet operator U in Eq. (1) and focus on the parameter regimes $\theta_1 \approx 0$ and $\theta_2 \approx \pi/2$. Under these conditions, the

momentum-space quasienergies are approximately $E_{\pm}\left(k_x,k_y\right) \simeq \pm\frac{\pi}{2} \pm \tilde{E}\left(k_x,k_y\right)$, where

$$\tilde{E}\left(k_x,k_y\right) = \theta_1 \cos\left(k_y - i\gamma_y - k_x + i\gamma_x\right) - \left(\frac{\pi}{2} - \theta_2\right)\cos\left(k_x - i\gamma_x + k_y - i\gamma_y\right). \tag{21}$$

The corresponding eigenstates are

$$|\psi_{\pm}(\boldsymbol{k})\rangle \simeq \begin{pmatrix} 1 \\ \mp e^{i(k_x - i\gamma_x - k_y + i\gamma_y)} \end{pmatrix}. \tag{22}$$

The local initial state is the uniform superposition of Bloch states in the upper band

$$\begin{aligned} |\psi(0)\rangle_2 &= |0\rangle \otimes |x=0,y=0\rangle - e^{\gamma_x-\gamma_y}|1\rangle \otimes |x=-1,y=1\rangle \\ &= \frac{1}{4\pi^2}\int_{-\pi}^{\pi}\int_{-\pi}^{\pi} \mathrm{d}k_x \mathrm{d}\,k_y |\psi_+(\boldsymbol{k})\rangle \otimes |\boldsymbol{k}\rangle. \end{aligned} \tag{23}$$

We further write the time-evolved wave function at time t as

$$|\psi(t)\rangle = \sum\nolimits_{x,y} \begin{pmatrix} (-i)^t \tilde{\psi}_{x,y}(t) \\ -(-i)^t \tilde{\psi}_{x+1,y-1}(t) \end{pmatrix} \otimes |x,y\rangle, \tag{24}$$

where

$$\tilde{\psi}_{x,y}(t) = \frac{1}{(2\pi)^2}\int_{-\pi}^{\pi}\int_{-\pi}^{\pi} \mathrm{d}k_x \mathrm{d}\,k_y e^{ik_x x + ik_y y - i\tilde{E}(k_x,k_y)}. \tag{25}$$

Defining the center-of-mass positions of the wave function as in Eq. (2), we have $x_{CM}(t) \simeq \frac{1}{2}a_x t^2 - \frac{1}{2}$ and $y_{CM}(t) \simeq \frac{1}{2}a_y t^2 + \frac{1}{2}$ for short-time dynamics, where the self-accelerations are given by $a_x = \frac{1}{\pi^2}\int_{-\pi}^{\pi} \mathrm{d}k_x \mathrm{d}\,k_y E_I \frac{\partial E_R}{\partial k_x}$ and $a_y = \frac{1}{\pi^2}\int_{-\pi}^{\pi} \mathrm{d}k_x \mathrm{d}\,k_y E_I \frac{\partial E_R}{\partial k_y}$. Here we defined $E_+(k_x,k_y) = E_R + iE_I$.

Apparently, the self-accelerations have a simple geometric interpretation in terms of the energy spectrum $E_+(k_x,k_y)$ in the complex plane. For instance, the acceleration along the x direction can be written as

$$a_x = \frac{2}{\pi}\int_{-\pi}^{\pi} \mathrm{d}\,k_y \mathcal{A}_x\left(k_y\right), \tag{26}$$

where

$$\mathcal{A}_x\left(k_y\right) := \frac{1}{2\pi}\int_{-\pi}^{\pi} \mathrm{d}\,k_x E_I \frac{\partial E_R}{\partial k_x}. \tag{27}$$

For a fixed value of k_y (taken as a parameter), the expression $\int_{-\pi}^{\pi} \mathrm{d}\,k_x E_I \frac{\partial E_R}{\partial k_x}$ is the area enclosed by the spectrum $E\left(k_x,k_y\right)$ in the complex plane as k_x traverses Brillouin zone. Alternatively, taking the integration over k_y into account, a_x is proportional to the volume enclosed by $2\pi\mathcal{A}_x\left(k_y\right)$ in the parameter space, as k_y traverses the Brillouin zone.

Finally, for the long-time dynamics, we have

$$x_{\mathrm{CM}}(t) \sim v_{m_x} t, \quad y_{\mathrm{CM}}(t) \sim v_{m_y} t, \tag{28}$$

where v_{m_x} and v_{m_y} in Eq. (10) are the drift velocities, corresponding to the location of the global maximum of $E_I(k_x,k_y)$.

Experimental scheme

We implement both one- and two-dimensional quantum walks by employing a time-multiplexed configuration, sending attenuated single-photon pulses (with a wavelength of 808 nm and a pulse width of 88 ps) through a fiber network. While each full cycle around the fiber loop represents a discrete time step, the built-in optical elements within the loop, such as the half-wave plates, polarization beam splitters, quarter-wave plates, realize the time-evolution operator U within each step. We encode external spatial modes through discretized temporal shifts, while internal coin-state degrees of freedom are encoded using photonic polarizations. With this experimental arrangement, we successfully carried out one-dimensional and two-dimensional quantum walks in the same experimental platform under various configurations (see the Supplementary Information Note 3).

In the scenario of initial state preparation, as detailed in the main manuscript, achieving the required initial excitation involves establishing an equally weighted superposition of Bloch eigenstates within a specific lattice band. However, our experimental constraints prevent the direct encoding of such a state, given its inclusion of excitations on both odd and even lattice sites beyond the capabilities of our setup. To address this limitation, it is crucial to recognize that during the evolution process, wave packets characterized by odd or even positions in the initial state do not interfere at each step. Leveraging this key property, we strategically divide our experiment into two distinct steps. In the first step, the initial excitation exclusively occupies either the even or odd lattice sites. Subsequently, we reconstruct the dynamics of the wave packet by capitalizing on the linearity inherent in the system (see the Supplementary Information Note 4).

Origin of self-acceleration in non-Hermitian dynamics

In an Hermitian system, according to the Ehrenfest theorem, a wave packet cannot accelerate in the absence of any external force. However, this is not the case for non-Hermitian systems[13,22]. To illustrate this point, let us consider for example the single-particle dynamics on a one-dimensional lattice with Hamiltonian in the physical space $\hat{H} = \hat{T} + V(x)$, where x is the lattice site position, $V(x)$ is the external potential, $\hat{T} = T(\hat{p}_x)$ is the kinetic energy operator, $\hat{p}_x = -i\partial_x$ is the momentum operator, and $T(p_x)$ is the energy dispersion curve of a given lattice band. For the standard Hatano–Nelson model, for instance, one has $T(p_x) = J\exp(ip_x + \gamma) + J\exp(-ip_x - \gamma)$, where $J\exp(\pm\gamma)$ are the asymmetric left/right hopping amplitudes.

For a given initial excitation of the system $|\psi_0\rangle$ at time $t = 0$, with $\langle\psi_0|\psi_0\rangle = 1$, the evolved wave function for early times is given by

$$|\psi_t\rangle = \exp(-i\hat{H}t)|\psi_0\rangle \simeq \left(1 - it\hat{H} - \frac{t^2}{2}\hat{H}^2\right)|\psi_0\rangle. \tag{29}$$

From this equation, one can readily calculate the time evolution of the mean position $\langle x\rangle = \langle\psi_t|x|\psi_t\rangle/\langle\psi_t|\psi_t\rangle$, up to the order $\sim t^2$, and the corresponding initial acceleration, $a_x = (\mathrm{d}^2\langle x\rangle/\mathrm{d}t^2)_{t=0}$, which reads explicitly

$$a_x = \langle 2\hat{H}^\dagger x\hat{H} - x\hat{H}^2 - \hat{H}^{\dagger 2}x\rangle_0 + 2\langle\hat{H}^\dagger - \hat{H}\rangle_0\langle\hat{H}^\dagger x - x\hat{H}\rangle_0. \tag{30}$$

In the above equation, $\langle\hat{A}\rangle_0 \equiv \langle\psi_0|\hat{A}\psi_0\rangle$ denotes the mean value of any operator $\hat{A}$ over the initial state $|\psi_0\rangle$. Let us now assume that there is not any external force, $V(x) = 0$, so that the Hamiltonian contains the kinetic energy term solely, $\hat{H} = \hat{T}$. Using the generalized commutation relation $[x,F(\hat{p}_x)] = i(\mathrm{d}F/\mathrm{d}\,p_x)$ for any function $F(p_x)$ of the momentum operator, one obtains

$$\begin{aligned} a_x = \langle x(2\hat{T}^\dagger\hat{T} - \hat{T}^2 - \hat{T}^{\dagger 2})\rangle_0 + 2i\langle\frac{\partial\hat{T}^\dagger}{\partial p_x}(\hat{T}^\dagger - \hat{T})\rangle_0 + \\ + 2\langle\hat{T}^\dagger - \hat{T}\rangle_0\langle\hat{T}^\dagger x - x\hat{T}\rangle_0. \end{aligned} \tag{31}$$

Clearly, in any Hermitian system $\hat{T}^\dagger = \hat{T}$, we necessarily have $a_x = 0$. Conversely, in a non-Hermitian system where $\hat{T}^\dagger \neq \hat{T}$, the acceleration a_x

is non-vanishing for rather arbitrary initial states $|\psi_0\rangle$, with its value dependent on the specific initial excitation.

Self-acceleration and the non-Hermitian skin effect

In one-dimensional models, there is a one-to-one correspondence between the transient self-acceleration, under suitable initial excitation of the lattice, and the non-Hermitian skin effect. In fact, the skin effect, that is, the localization of a macroscopic number of eigenstates near the boundaries, appears rather generally whenever the Hamiltonian displays a point-gap topology in the PBC energy spectrum[14,15]. In the presence of the point-gap topology, the area $\mathcal{A}$, which is proportional to the self-acceleration, is necessarily non-vanishing. Additionally, we can have an intuitive explanation for self-acceleration from the skin effect. Let us consider a single-band system and single-site initial excitation of the lattice at $t = 0$. Clearly, the initial mean speed of the wave packet is zero, as all momenta k within the Brillouin zone are equally excited. Owing to the non-Hermitian skin effect, Bloch modes displaying opposite group velocities are differently damped or amplified, and their unbalanced interference yields a deformation of the wave packet spreading and a directed transport at long times, characterized by a non-vanishing drift velocity v_m. This implies that the wave packet must necessarily undergo acceleration to attain a final non-zero speed. The resulting self-acceleration can be thus explained as an unbalanced interference effects between spectral wave packet components displaying opposite group velocities.

In two-dimensional systems, the non-Hermitian skin effect can depend on the geometry of the boundaries, and it is thus clear that the bulk dynamics of a wave packet alone (including transient self-acceleration and long-time drift motion), cannot uniquely determine the behavior of these boundary-dependent systems. Indeed, a recent work proved that, in higher dimensions, the non-Hermitian skin effect is a universal phenomenon observed for almost every local non-Hermitian Hamiltonian that displays a finite spectral area under the PBC, and when the shape of the open boundaries are taken without any special symmetries[16]. A distinction between generalized reciprocal and non-reciprocal skin effect has also been introduced[16], depending on whether the current in the system is vanishing or not, respectively.

In our two-dimensional non-Hermitian quantum walk, the non-vanishing self-acceleration clearly corresponds to a non-vanishing current, and thus the skin effect is of the latter type and is observable for arbitrary boundary shapes. The vanishing of the self-acceleration in a two-dimensional system does not necessarily imply the absence of the non-Hermitian skin effect under *arbitrary* shape of the boundaries, albeit it can disappear for a *specific* shape of the boundaries. To clarify this point, let us consider for example the two-dimensional square lattice described by the Bloch Hamiltonian

$$H(k_x,k_y) = J_x \cos k_x + iJ_y \cos k_y, \tag{32}$$

with real (Hermitian) hopping amplitude J_x along the x direction, and imaginary (non-Hermitian) hopping amplitude iJ_y along the y direction. Note that in this non-Hermitian model, the hopping amplitudes are reciprocal, and from the formulas of a_x and a_y, it readily follows that $a_x = a_y = 0$, that is, transient self-acceleration in the bulk is absent. In this model, the non-Hermitian skin effect disappears for a square geometry of the boundaries due to the existence of two mirror symmetries. However, skin modes appear under different boundaries which break these mirror symmetries[16].

Data availability

The data that support the findings of this study are available from the corresponding authors upon requests.

Code availability

The codes that support the findings of this study are available from the corresponding authors upon requests.

References

1. Kenkre, V. M. Relations among theories of excitation transfer. II. Influence of spectral features on exciton motion. *Phys. Rev. B* **12**, 2150 (1975).
2. Eberly, J. H., Narozhny, N. B. & Sanchez-Mondragon, J. J. Periodic spontaneous collapse and revival in a simple quantum model. *Phys. Rev. Lett.* **44**, 1323 (1980).
3. Chang, M.-C. & Niu, Q. Berry phase, hyperorbits, and the Hofstadter spectrum: semiclassical dynamics in magnetic Bloch bands. *Phys. Rev. B* **53**, 7010 (1996).
4. Upreti, L. K. et al. Topological swing of Bloch oscillations in quantum walks. *Phys. Rev. Lett.* **125**, 186804 (2020).
5. Genov, D. A., Zhang, S. & Zhang, X. Mimicking celestial mechanics in metamaterials. *Nat. Phys.* **5**, 687–692 (2009).
6. Neto, A. C., Guinea, F., Peres, N. M. R., Novoselov, K. S. & Geim, A. K. The electronic properties of graphene. *Rev. Mod. Phys.* **81**, 109 (2009).
7. Tarruell, L., Greif, D., Uehlinger, T., Jotzu, G. & Esslinger, T. Creating, moving and merging Dirac points with a Fermi gas in a tunable honeycomb lattice. *Nature* **483**, 302–305 (2012).
8. Jacqmin, T. et al. Direct observation of Dirac cones and a flatband in a honeycomb lattice for polaritons. *Phys. Rev. Lett.* **112**, 116402 (2014).
9. Guarneri, I. & Mantica, G. Multifractal energy spectra and their dynamical implications. *Phys. Rev. Lett.* **73**, 3379 (1994).
10. Bender, C. M. Making sense of non-Hermitian Hamiltonians. *Rep. Prog. Phys.* **70**, 947 (2007).
11. Breuer, H. P. & Petruccione, F. *The Theory of Open Quantum Systems* (Oxford University Press, 2007).
12. Ashida, Y., Gong, Z. & Ueda, M. Non-Hermitian physics. *Adv. Phys.* **69**, 249–435 (2020).
13. Gong, Z. et al. Topological phases of Non-Hermitian systems. *Phys. Rev. X* **8**, 031079 (2018).
14. Zhang, K., Yang, Z. & Fang, C. Correspondence between winding numbers and skin modes in non-Hermitian systems. *Phys. Rev. Lett.* **125**, 126402 (2020).
15. Okuma, N., Kawabata, K., Shiozaki, K. & Sato, M. Topological origin of non-Hermitian skin effects. *Phys. Rev. Lett.* **124**, 086801 (2020).
16. Zhang, K., Yang, Z. & Fang, C. Universal non-Hermitian skin effect in two and higher dimensions. *Nat. Commun.* **13**, 2496 (2022).
17. Bergholtz, E. J., Budich, J. C. & Kunst, F. K. Exceptional topology of non-Hermitian systems. *Rev. Mod. Phys.* **93**, 015005 (2021).
18. Wanjura, C. C., Brunelli, M. & Nunnenkamp, A. Topological framework for directional amplification in driven-dissipative cavity arrays. *Nat. Commun.* **11**, 3149 (2020).
19. Wanjura, C. C., Brunelli, M. & Nunnenkamp, A. Correspondence between non-Hermitian topology and directional amplification in the presence of disorder. *Phys. Rev. Lett.* **127**, 213601 (2021).
20. Brunelli, M., Wanjura, C. C. & Nunnenkamp, A. Restoration of the non-Hermitian bulk-boundary correspondence via topological amplification. *SciPost Phys.* **15**, 173 (2023).
21. Slim, J. J. et al. Optomechanical realization of the bosonic Kitaev-Majorana chain. Preprint at https://arxiv.org/abs/2309.05825 (2023).
22. Graefe, E. M., Honing, M. & Korsch, H. J. Classical limit of non-Hermitian quantum dynamics – a generalised canonical structure. *J. Phys. A* **43**, 075306 (2010).
23. Graefe, E.-M. & Schubert, R. Wave-packet evolution in non-Hermitian quantum systems. *Phys. Rev. A* **83**, 060101(R) (2011).

24. Holmes, K., Rehman, W., Malzard, S. & Graefe, E.-M. Husimi dynamics generated by non-Hermitian Hamiltonians. *Phys. Rev. Lett.* **130**, 157202 (2023).
25. Yao, S. & Wang, Z. Edge states and topological invariants of non-Hermitian systems. *Phys. Rev. Lett.* **121**, 086803 (2018).
26. Kawabata, K., Shiozaki, K., Ueda, M. & Sato, M. Symmetry and topology in non-Hermitian physics. *Phys. Rev. X* **9**, 041015 (2019).
27. Zhou, H. & Lee, J. Y. Periodic table for topological bands with non-Hermitian symmetries. *Phys. Rev. B* **99**, 235112 (2019).
28. Xiao, L. et al. Observation of non-Bloch parity-time symmetry and exceptional points. *Phys. Rev. Lett.* **126**, 230402 (2021).
29. Jezequel, L. & Delplace, P. Non-Hermitian spectral flows and Berry-Chern monopoles. *Phys. Rev. Lett.* **130**, 066601 (2023).
30. Xue, W.-T., Hu, Y.-M., Song, F. & Wang, Z. Non-Hermitian edge burst. *Phys. Rev. Lett.* **128**, 120401 (2022).
31. Xiao, L. et al. Observation of non-Hermitian edge burst in quantum dynamics. Preprint at https://arxiv.org/abs/2303.12831 (2023).
32. Yuce, C. & Ramezani, H. Non-Hermitian edge burst without skin localization. *Phys. Rev. B* **107**, L140302 (2023).
33. Kunst, F. K., Edvardsson, E., Budich, J. C. & Bergholtz, E. J. Biorthogonal bulk-boundary correspondence in non-Hermitian systems. *Phys. Rev. Lett.* **121**, 026808 (2018).
34. Yokomizo, K. & Murakami, S. Non-Bloch band theory of non-Hermitian systems. *Phys. Rev. Lett.* **123**, 066404 (2019).
35. Yang, Z., Zhang, K., Fang, C. & Hu, J. Non-Hermitian bulk-boundary correspondence and auxiliary generalized Brillouin zone theory. *Phys. Rev. Lett.* **125**, 226402 (2020).
36. Guo, C.-X., Liu, C.-H., Zhao, X.-M., Liu, Y. & Chen, S. Exact solution of non-Hermitian systems with generalized boundary conditions: Size-dependent boundary effect and fragility of the skin effect. *Phys. Rev. Lett.* **127**, 116801 (2021).
37. Longhi, S. Self-healing of non-Hermitian topological skin modes. *Phys. Rev. Lett.* **128**, 157601 (2022).
38. Wan, L.-L. & Lü, X.-Y. Quantum-squeezing-induced point-gap topology and skin effect. *Phys. Rev. Lett.* **130**, 203605 (2023).
39. Weidemann, S., Kremer, M., Longhi, S. & Szameit, A. Topological triple phase transition in non-Hermitian Floquet quasicrystals. *Nature* **601**, 354–359 (2022).
40. Wang, K. et al. Generating arbitrary topological windings of a non-Hermitian band. *Science* **371**, 1240–1245 (2021).
41. Li, L., Lee, C. H., Mu, S. & Gong, J. Critical non-Hermitian skin effect. *Nat. Commun.* **11**, 5491 (2020).
42. Song, F., Yao, S. & Wang, Z. Non-Hermitian skin effect and chiral damsping in open quantum systems. *Phys. Rev. Lett.* **123**, 170401 (2019).
43. Haga, T., Nakagawa, M., Hamazaki, R. & Ueda, M. Liouvillian skin effect: slowing down of relaxation processes without gap closing. *Phys. Rev. Lett.* **127**, 070402 (2021).
44. Mori, T. & Shirai, T. Symmetrized Liouvillian gap in Markovian open quantum systems. *Phys. Rev. Lett.* **130**, 230404 (2023).
45. Xiao, L. et al. Non-Hermitian bulk-boundary correspondence in quantum dynamics. *Nat. Phys.* **16**, 761–766 (2020).
46. Helbig, T. et al. Generalized bulk-boundary correspondence in non-Hermitian topolectrical circuits. *Nat. Phys.* **16**, 747–750 (2020).
47. Ghatak, A., Brandenbourger, M., Van Wezel, J. & Coulais, C. Observation of non-Hermitian topology and its bulk-edge correspondence in an active mechanical metamaterial. *Proc. Natl Acad. Sci.* **117**, 29561 (2020).
48. Weidemann, S. et al. Topological funneling of light. *Science* **368**, 311–314 (2020).
49. Wang, W., Wang, X. & Ma, G. Non-Hermitian morphing of topological modes. *Nature* **608**, 50–55 (2022).
50. Liang, Q. et al. Dynamic signatures of non-Hermitian skin effect and topology in ultracold atoms. *Phys. Rev. Lett.* **129**, 070401 (2022).
51. Hofmann, T. et al. Reciprocal skin effect and its realization in a topolectrical circuit. *Phys. Rev. Res.* **2**, 023265 (2020).
52. Zou, D. et al. Observation of hybrid higher-order skin-topological effect in non-Hermitian topolectrical circuits. *Nat. Commun.* **12**, 7201 (2021).
53. Zhang, X., Tian, Y., Jiang, J.-H., Lu, M.-H. & Chen, Y.-F. Observation of higher-order non-Hermitian skin effect. *Nat. Commun.* **12**, 5377 (2021).
54. Lin, R., Tai, T. & Li, L. et al. Topological non-Hermitian skin effect. *Front. Phys.* **18**, 53605 (2023).
55. Longhi, S. Probing non-Hermitian skin effect and non-Bloch phase transitions. *Phys. Rev. Res.* **1**, 023013 (2019).
56. Longhi, S. Non-Hermitian skin effect and self-acceleration. *Phys. Rev. B* **105**, 245143 (2022).
57. Lin, Q. et al. Observation of non-Hermitian topological Anderson insulator in quantum dynamics. *Nat. Commun.* **13**, 3229 (2022).
58. Lin, Q. et al. Topological phase transitions and mobility edges in non-Hermitian quasicrystals. *Phys. Rev. Lett.* **129**, 113601 (2022).
59. Lin, Q., Yi, W. & Xue, P. Manipulating directional flow in a two-dimensional photonic quantum walk under a synthetic magnetic field. *Nat. Commun.* **14**, 6283 (2023).
60. Schreiber, A. et al. A 2D quantum walk simulation of two-particle dynamics. *Science* **336**, 55–58 (2012).
61. Chen, C. et al. Topological spin texture of chiral edge states in photonic two-dimensional quantum walks. *Phys. Rev. Lett.* **129**, 046401 (2022).

Acknowledgements

This work has been supported by the National Key R&D Program of China (Grant No. 2023YFA1406701) and National Natural Science Foundation of China (Grant Nos. 12025401, 92265209, 12374479, 11974331, 12104009 and 12104036).

Author contributions

P.X. supervised the project, designed the experiments, analyzed the results, and wrote part of the paper. Q.L. performed the experiments with the contribution from K.K.W. and L.X. S.L. developed the theoretical aspects and revised the paper. W.Y. performed the theoretical analysis and wrote part of the paper.

Competing interests

The authors declare no competing interests.

Additional information

Supplementary information The online version contains supplementary material available at https://doi.org/10.1038/s41467-024-48815-y.

Correspondence and requests for materials should be addressed to Peng Xue, Stefano Longhi or Wei Yi.

Peer review information *Nature Communications* thanks Alessio D'Errico, Roberto de J. León-Montiel, and the other, anonymous, reviewer(s) for their contribution to the peer review of this work. A peer review file is available.

Reprints and permissions information is available at http://www.nature.com/reprints

Publisher's note Springer Nature remains neutral with regard to jurisdictional claims in published maps and institutional affiliations.

Open Access This article is licensed under a Creative Commons Attribution 4.0 International License, which permits use, sharing, adaptation, distribution and reproduction in any medium or format, as long as you give appropriate credit to the original author(s) and the source, provide a link to the Creative Commons licence, and indicate if changes were made. The images or other third party material in this article are included in the article's Creative Commons licence, unless indicated otherwise in a credit line to the material. If material is not included in the article's Creative Commons licence and your intended use is not permitted by statutory regulation or exceeds the permitted use, you will need to obtain permission directly from the copyright holder. To view a copy of this licence, visit http://creativecommons.org/licenses/by/4.0/.

© The Author(s) 2024

SUPPLEMENTARY INFORMATION FOR "SELF ACCELERATION FROM SPECTRAL GEOMETRY IN DISSIPATIVE QUANTUM-WALK DYNAMICS"

In this Supplementary Information, we provide some technical and experimental details.

Supplementary Note 1 - Derivation of the Floquet operator U and the effective Hamiltonian

As mentioned in the main text, in the one-dimensional quantum walk, the Floquet operator reads $U = S_x M_x R(\theta)$. As all the operators can be expressed by Pauli matrices, the time-evolution operator can be also written as

$$\begin{aligned} U(k) &= d_0(k)\sigma_0 + id_x\sigma_x + id_y(k)\sigma_y + id_z(k)\sigma_z \\ d_0(k) &= \cos(\theta)\cos(-i\gamma_x + k), \\ d_x(k) &= \sin(\theta)\cos(-i\gamma_x + k), \\ d_y(k) &= -\sin(\theta)\sin(-i\gamma_x + k), \\ d_z(k) &= \cos(\theta)\sin(-i\gamma_x + k). \end{aligned} \tag{1}$$

The effective Hamiltonian is defined through the relation $U = e^{-iH}$, which in the quasi-momentum space takes the form

$$H = \int_{-\pi}^{\pi} \mathrm{d}\boldsymbol{k}\, [E(\boldsymbol{k})\mathbf{n}(\boldsymbol{k})\cdot\sigma] \otimes |\boldsymbol{k}\rangle\langle\boldsymbol{k}|, \tag{2}$$

with

$$\mathbf{n}(k) = \frac{1}{\sin E(k)} \begin{pmatrix} -\sin(\theta)\cos(k - i\gamma_x) \\ \sin(\theta)\sin(k - i\gamma_x) \\ -\cos(\theta)\sin(k - i\gamma_x) \end{pmatrix}. \tag{3}$$

Here the quasienergies are given by $E_\pm(k) = \pm\arccos[\cos\theta\cos(k - i\gamma_x)]$, which are the eigenvalues of H.

Similarly, for the two-dimensional case, we have

$$\begin{aligned} \mathbf{n}(\boldsymbol{k}) &= \mathbf{n}(k_x, k_y) \\ &= \frac{1}{\sin E(k_x, k_y)} \begin{pmatrix} -\cos(k_x + k_y - i\gamma_x - i\gamma_y)\cos(\theta_2)\sin(\theta_1) - \cos(k_x + k_y - i\gamma_x + i\gamma_y)\cos(\theta_1)\sin(\theta_2) \\ \sin(k_x + k_y - i\gamma_x - i\gamma_y)\cos(\theta_2)\sin(\theta_1) - \sin(k_x + k_y - i\gamma_x + i\gamma_y)\cos(\theta_1)\sin(\theta_2) \\ -\sin(k_x + k_y - i\gamma_x - i\gamma_y)\cos(\theta_2)\cos(\theta_1) - \sin(k_x + k_y - i\gamma_x + i\gamma_y)\sin(\theta_1)\sin(\theta_2) \end{pmatrix}, \end{aligned} \tag{4}$$

where the quasienergy is

$$E(k_x, k_y) = \pm\arccos\left[\theta_1\cos(k_y - i\gamma_y - k_x + i\gamma_x) - \left(\frac{\pi}{2} - \theta_2\right)\cos(k_x - i\gamma_x + k_y - i\gamma_y)\right]. \tag{5}$$

Supplementary Note 2 - Correspondence between spectral topology and self-acceleration in one-dimensional lattices

1. Single-band lattice models

For the most exemplary class of NH lattice models, namely those featuring a single band with a point gap and no symmetry (see for example [1]), there is a one-to-one correspondence between non-trivial spectral point gap topology and self-acceleration, namely the following theorem 1 holds:

In any single-band NH lattice model, the early-time acceleration a_x of the center-of-mass wave packet under initial single-site excitation of the lattice is proportional to the spectral area $\mathcal{A}$ enclosed by the complex PBC energy spectrum $H(k)$ in the complex plane, namely

$$a_x = \frac{2}{\pi}\mathcal{A}. \tag{6}$$

The proof of such a general theorem was given in the earlier theoretical paper [2] and it is therefore not repeated here. Note that the above result clearly provides a universal correspondence between self-acceleration and spectral topology in generic one-band NH lattice systems without any special symmetry. Note also that, since the initial excitation condition is independent of the Hamiltonian $H(k)$, the dynamical probing method provides a universal tool for testing the spectral topology of the system that does not require any *a priori* knowledge of the system Hamiltonian.

2. Many-band lattice models

The photonic quantum walk setup used in our experiments is inherently a two-band system, and thus it is important to extend theorem 1 above to the multiband case. To this aim, let us consider an M-band NH lattice system, so that each unit cell of the lattice comprises M sublattice sites. Let us indicate by $a_n(t)$, $b_n(t)$, $c_n(t)$, ... the amplitudes of the wave function at the M sites in the n-th unit celll of the lattice. Let $H(k)$ be the $M \times M$ Bloch Hamiltonian of the system, and let us indicate by $E_\beta(k)$ and $(A_\beta(k), B_\beta(k), C_\beta(k), ...)^T$, the eigenvalues and corresponding eigenvectors of $H(k)$ ($\beta = 1, 2, ..., M$), respectively. Specifically, we have

$$E_\beta(k) \begin{pmatrix} A_\beta(k) \\ B_\beta(k) \\ C_\beta(k) \\ ... \end{pmatrix} = H(k) \begin{pmatrix} A_\beta(k) \\ B_\beta(k) \\ C_\beta(k) \\ ... \end{pmatrix} \tag{7}$$

with $\beta = 1, 2, ..., M$. Clearly, there is some arbitrariness in the choice of $A_\beta(k)$, $B_\beta(k)$, ..., since they are defined up to an arbitrary complex factor that may depend on the Bloch wave number k. After a suitable choice of such a multiplication factor, it can be readily shown that the amplitudes $A_\beta k)$, $B_\beta(k)$, ... can be chosen to satisfy the following conditions

$$|A_\beta(k)|^2 + |B_\beta(k)|^2 + |C_\beta(k)|^2 + ... = 1 \ , \ \ A_l^*(k)\frac{dA_\beta}{dk} + B_\beta^*(k)\frac{dB_\beta}{dk} + ... = 0. \tag{8}$$

for any $\beta = 1, 2, 3, ..., M$. The first condition in Eq.(8) corresponds to wave function normalization, whereas the second condition in Eq.(8) corresponds to the gauge choice such that the diagonal elements of Berry connection vanish. Since the Hamiltonian $H(k)$ is non-Hermitian, the eigeneneriges $E_\beta(k)$ and the corresponding eigenvectors are not necessarily single-valued functions of the Bloch wave number k, i.e., if we continuously follow the change of the eigenvalue $E_\beta(k)$, as k continuously changes from $k = -\pi$ to $k = \pi$ along the Brillouin zone, we can have a flip of eigenvalues and eigenvectors at the end of the cycle. Only after M cycles are the initial eigenenergy and eigenstate retrieved. The nontrivial energy-surface topology is typically associated with the fact that the cycle encloses one or more exceptional points (see for instance [3–6]). We say that the multi-band system has a trivial energy-surface topology whenever there is no eigenenergies and eigenevector flipping after one cycle (when k continuously change from $k = -\pi$ to $k = \pi$ along the Brillouin zone).

The mean position of a wave packet at time t in the physical space is given by

$$\langle n(t) \rangle = \frac{\sum_n n(|a_n(t)|^2 + |b_n(t)|^2 + |c_n(t)|^2 + ...)}{\sum_n (|a_n(t)|^2 + |b_n(t)|^2 + |c_n(t)|^2 + ...)}. \tag{9}$$

The following theorem 2 can be stated:
For a given band index α of the lattice ($\alpha = 1, 2, ..., M$), let us prepare the system at the initial time $t = 0$ in the state

$$a_n(0) = \frac{1}{2\pi}\int_{-\pi}^{\pi} A_\alpha(k)\exp(ikn) \ , \ b_n(0) = \frac{1}{2\pi}\int_{-\pi}^{\pi} B_\alpha(k)\exp(ikn) \ , \ c_n(0) = \frac{1}{2\pi}\int_{-\pi}^{\pi} C_\alpha(k)\exp(ikn) \ ... \tag{10}$$

where the Bloch eigenevector amplitudes $A_\alpha(k)$, $B_\alpha(k)$, ... are assumed to satisfy Eq. (8). Then, if the system has a trivial energy-surface topology, the early-time acceleration a_x of the wave packet center of mass is given by

$$a_x = \frac{2}{\pi}\mathcal{A}_\alpha, \tag{11}$$

where $\mathcal{A}_\alpha$ is the area enclosed by the curve $E_\alpha(k)$ in the complex plane.

Proof. To prove theorem 2, let us first observe that the most general solution to the time-dependent Schrödinger equation in the multi-band lattice system reads

$$\begin{pmatrix} a_n(t) \\ b_n(t) \\ c_n(t) \\ ... \end{pmatrix} = \sum_{\beta=1}^{M} \int_{-\pi}^{\pi} dk F_\beta(k) \begin{pmatrix} A_\beta(k) \\ B_\beta(k) \\ C_\beta(k) \\ ... \end{pmatrix} \exp[ikn - iE_\beta(k)], \tag{12}$$

where the spectral amplitudes $F_\beta(k)$ are determined by the initial excitation of the system at time $t = 0$. Let us assume that the initial state is the one defined by Eq.(10), which corresponds to the choice $F_\beta(k) = (1/2\pi)\delta_{\alpha,\beta}$ for the spectral amplitude. Hence one has

$$\begin{pmatrix} a_n(t) \\ b_n(t) \\ c_n(t) \\ ... \end{pmatrix} = \frac{1}{2\pi} \int_{-\pi}^{\pi} dk \begin{pmatrix} A_\alpha(k) \\ B_\alpha(k) \\ C_\alpha(k) \\ ... \end{pmatrix} \exp[ikn - iE_\alpha(k)]. \tag{13}$$

From Eq.(13), one can calculate the terms $\sum_n |a_n(t)|^2$, $\sum_n |b_n(t)|^2$, $\sum_n |c_n(t)|^2$,.. and $\sum_n n|a_n(t)|^2$, $\sum_n n|b_n(t)|^2$, $\sum_n n|c_n(t)|^2$,... . For example, one has

$$\sum_n |a_n(t)|^2 = \frac{1}{4\pi^2} \int_{-\pi}^{\pi} dk \int_{-\pi}^{\pi} dk' A_\alpha(k) A_\alpha^*(k') S(k-k') \exp\left[-itE_\alpha(k)t + iE_\alpha^*(k')t\right], \tag{14}$$

where we set

$$S(k-k') = \sum_n \exp[i(k-k')n]. \tag{15}$$

It follows that, in the range of variability of k and k',

$$S(k-k') = 2\pi\delta(k-k'), \tag{16}$$

and thus

$$\sum_n |a_n(t)|^2 = \frac{1}{2\pi} \int_{-\pi}^{\pi} dk |A_\alpha(k)|^2 \exp[2E_{I\alpha}(k)t], \tag{17}$$

where $E_{I\alpha}(k)$ is the imaginary part of the complex energy $E_\alpha(k)$. Similar expressions are found for $\sum_n |b_n(t)|^2$, $\sum_n |c_n(t)|^2$, ..., namely

$$\sum_n |b_n(t)|^2 = \frac{1}{2\pi} \int_{-\pi}^{\pi} dk |B_\alpha(k)|^2 \exp[2E_{I\alpha}(k)t] \ , \ \sum_n |c_n(t)|^2 = \frac{1}{2\pi} \int_{-\pi}^{\pi} dk |C_\alpha(k)|^2 \exp[2E_{I\alpha}(k)t] \ , \ ... \tag{18}$$

Taking Eq. (8) into account, from Eqs. (17) and (18), one then obtains

$$\sum_n (|a_n(t)|^2 + |b_n(t)|^2 + |c_n(t)|^2 + ...) = \frac{1}{2\pi} \int_{-\pi}^{\pi} dk \exp[2E_{I\alpha}(k)t]. \tag{19}$$

Let us now calculate $\sum_n n|a_n(t)|^2$. One has

$$\sum_n n|a_n(t)|^2 = -i\frac{1}{4\pi^2} \int_{-\pi}^{\pi} dk' \int_{-\pi}^{\pi} dk A_\alpha(k) A_\alpha^*(k') \exp\left[-itE_\alpha(k)t + iE_\alpha^*(k')t\right] . \frac{\partial S(k-k')}{\partial k} \tag{20}$$

After integration by parts and taking into account that $E_\alpha(\pi) = E_\alpha(-\pi)$ and $A_\alpha(\pi) = A_\alpha(-\pi)$ owing to the trivial energy surface topology, one readily obtains

$$\sum_n n|a_n(t)|^2 = \frac{i}{2\pi} \int_{-\pi}^{\pi} dk \left(A_\alpha^* \frac{dA_\alpha}{dk} - it|A_\alpha(k)|^2 \frac{dE_\alpha}{dk} \right) \exp[2E_{I\alpha}(k)t]. \tag{21}$$

Similar expressions are found for $\sum_n n|b_n(t)|^2$, $\sum_n n|c_n(t)|^2$, ..., namely

$$\sum_n n|b_n(t)|^2 = \frac{i}{2\pi}\int_{-\pi}^{\pi} dk \left(B_\alpha^* \frac{dB_\alpha}{dk} - it|B_\alpha(k)|^2 \frac{dE_\alpha}{dk} \right) \exp[2E_{I\alpha}(k)t],$$
$$\sum_n n|c_n(t)|^2 = \frac{i}{2\pi}\int_{-\pi}^{\pi} dk \left(C_\alpha^* \frac{dC_\alpha}{dk} - it|C_\alpha(k)|^2 \frac{dE_\alpha}{dk} \right) \exp[2E_{I\alpha}(k)t], \quad (22)$$
$$\text{... ...}$$

Taking into account of Eq. (8), from Eqs.(21) and (22) one obtains

$$\sum_n n(|a_n(t)|^2 + |b_n(t)|^2 + |c_n(t)|^2 + ...) = \frac{t}{2\pi}\int_{-\pi}^{\pi} dk \frac{dE_\alpha}{dk} \exp[2E_{I\alpha}(k)t]. \quad (23)$$

Using Eqs. (19) and (23), the evolution of the wave packet center of mass [Eq.(9)] finally reads

$$\langle n(t)\rangle = \frac{t\int_{-\pi}^{\pi} dk \frac{dE_\alpha}{dk} \exp[2E_{I\alpha}(k)t]}{\int_{-\pi}^{\pi} dk \exp[2E_{I\alpha}(k)t]}, \quad (24)$$

which holds at any given instant t. In particular, in the early time dynamics with $t \to 0$, the above expression can be written as a series expansion in powers of t. At the lowest order, one obtains

$$\langle n(t)\rangle \simeq \frac{t^2}{\pi}\mathcal{A}_\alpha, \quad (25)$$

where we have set

$$\mathcal{A}_\alpha = \int_{-\pi}^{\pi} dk \frac{dE_{R\alpha}}{dk} E_{I\alpha}(k), \quad (26)$$

and $E_{R\alpha}(k)$, $E_{I\alpha}(k)$ are the real and imaginary parts of the energy $E_\alpha(k)$, respectively. Clearly, $\mathcal{A}_\alpha$ corresponds to the area enclosed by the energy $E_\alpha(k)$ in the complex plane as k traverses the Brillouin zone. Equation (25) shows that, at early time, the wave packet center of mass displays an accelerated motion with an acceleration $a_x = 2\mathcal{A}_\alpha/\pi$, which thus provides a dynamical measure of the spectral geometry of the α-th lattice band. This concludes the proof of theorem 2.

It should be mentioned that, as compared to the single-band case, in multi-band lattices the initial state preparation of the system [Eq.(10)] requires some knowledge of the Hamiltonian and can be in practice challenging. However, for narrow-band systems where the bands are spaced in complex energy plane by wide gaps, such as when the detuning of the on-site potentials at sites a, b, c, ... are much larger than the hopping amplitudes, in the appropriate basis the required initial excitation basically reduces to single-site excitation as in the single-band case, thus relaxing the condition of prior knowledge of the Hamiltonian. In our experiment, we are dealing with a two-band system and the narrow-band regime is attained for a coin angle θ close to $\pi/2$. The corresponding initial excitation of the system is very simple, as discussed in the Method section, and we can accurately estimate the spectral areas from wave-packet self-acceleration measurements.

Supplementary Note 3 - Experimental scheme

We implement quantum walks by employing a time-multiplexed configuration, where the external spatial modes are encoded through discretized temporal shifts, and the internal coin-state degrees of freedom are encoded using photonic polarizations (Fig. 1). With this experimental arrangement, we successfully carried out one-dimensional and two-dimensional quantum walks in the same experimental platform under various configurations, as demonstrated in the following.

The overall architecture is that of a fiber network, through which attenuated single-photon pulses with a wavelength of 808 nm and a pulse width of 88ps are sent, with each full cycle around the network representing a discrete time step. Laser pulses are attenuated by neutral density filters, which effectively reduce the energy of the laser pulses to the single-photon level at the detection stage. This step aims to maintain an average photon number per pulse below 2.6×10^{-4} to minimize the probability of multi-photon events. The input intensity of the initial laser pulse can be increased when we aim to obtain amplitude distribution of quantum walks after larger numbers of steps.

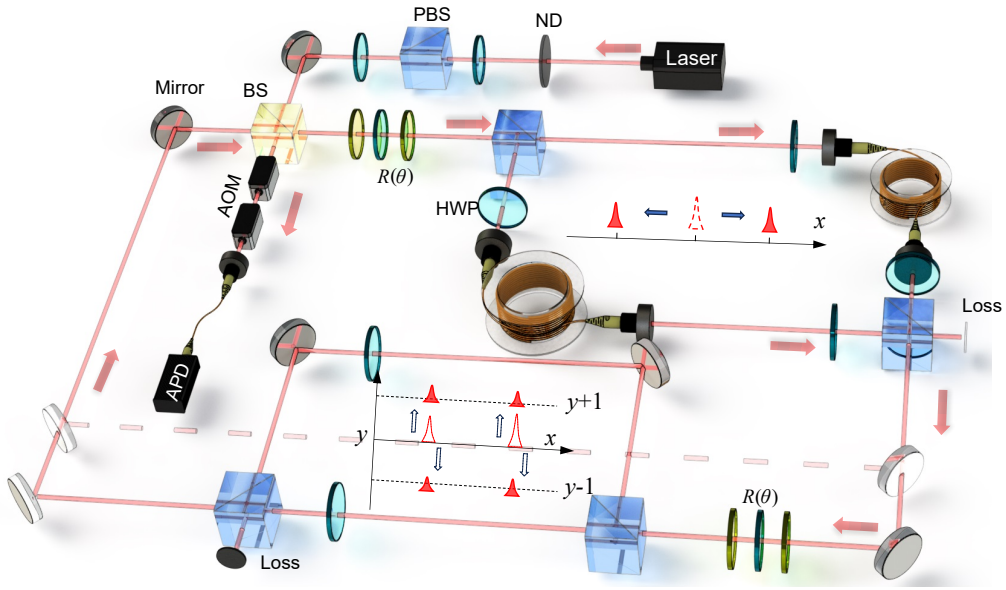

Supplementary Figure 1. **A time-multiplexed implementation of the two-dimensional photonic quantum walk.** The process involves splitting photonic wave packets using a polarizing beam splitter (PBS) and guiding them through a pair of single-mode fibers (SMF) to achieve a temporal step in the x direction. Similarly, a temporal step in the y direction is achieved using another two-PBS loop in free space. At each step, partial photons are coupled out and directed towards avalanche photodiodes (APDs) for polarization resolving detection of their arrival times. ND: neutral density filter; AOM: optical switch acousto-optic modulator.

The coin states $\{|0\rangle, |1\rangle\}$ are encoded in the photon polarizations $\{|H\rangle, |V\rangle\}$. The single-photon pulse act as the walker, exhibiting distribution across multiple temporal modes. This is achieved by building path-dependent time delays into the four different paths (labeled $x \pm 1$ and $y \pm 1$) in Fig. 1 within the network. Specifically, for two-dimensional quantum walks, the temporal modes were separated by two different time scales: 80ns in the x-dimension and 4.83ns in the y-dimension. For the one-dimensional quantum walk, the temporal modes were solely distributed along the x-dimension.

To implement the two-dimensional quantum walk, we rewrite the time-evolution operator as $U^t = e^{\gamma_x \gamma_y t} U_E^t$, where

$$U_E^t = M_y^{'} S_y R(\theta_2) M_x^{'} S_x R(\theta_1) \tag{27}$$

with $M_i^{'} = e^{-|\gamma_i|} M_i, i = x, y$.

The coin state is initialized after single-photon pulses pass through a polarizing beam splitter (PBS) and a half-wave plate (HWP). Subsequently, the photons are coupled in and out from a time-multiplexed configuration via a beam splitter (BS) with a reflectivity of 3%. The coin operator $R(\theta_{1(2)})$ is implemented by the sandwich-type set of wave plates (QWP-HWP-QWP), where QWP is the abbreviation of quarter-wave plate. To implement the shift operators, PBSs separate the photons with different polarizations and direct them into the two-fiber loop (S_x) or the free-space Mach-Zehnder interferometer (S_y). Specifically, the difference between two distinct fiber lengths (270m and 287.03m) are used to realize the polarization-dependent time delay 80ns in the x-dimension. The corresponding time difference in the y direction is 4.83ns, which is introduced by a 1.61m free space path difference of the free-space Mach-Zehnder interferometer. Importantly, the coherence of single-photon pulses is inherently preserved by the interference condition required for the single-particle quantum walk.

To implement the loss operation $M_x^{'}$, two HWPs are introduced into each fiber loop. The ones at the input and output ends of the fiber are also used to keep the polarizations of the single-photon pulses unchanged. For $\gamma_x > 0$, we adjust the angle of the HWP in the $x+1$ path satisfying $\cos\frac{\theta}{2} = e^{-2\gamma_x}$, the part of photons $1 - e^{-4\gamma_x}$ are transmitted by the second PBS, and leak out of the setup. For $\gamma_x < 0$, we set the angle of the HWP on the $x-1$ path to satisfy $\cos\frac{\theta}{2} = e^{2\gamma_x}$ and the part of photons $1 - e^{4\gamma_x}$ subsequently leak out of the setup. The loss operator $M_y^{'}$ is realized with the same method.

Arrival time is recorded by avalanche photodiodes (APDs), aided by an acoustic-optical modulator (AOM) that functions as an optical switch to eliminate unwanted pulses. The time-resolved pulses within the window are recorded

and translated to the corresponding spatial position of the walker. We measure the probability distribution of quantum walks

$$P(x,y,t)=\frac{|\langle\psi(x,y,t)|\psi(x,y,t)\rangle|}{\sum_{x,y}|\langle\psi(x,y,t)|\psi(x,y,t)\rangle|}=\frac{N(x,y,t)}{\sum_{x,y}N(x,y,t)}, \tag{28}$$

where $N(x,y,t)$ is the total photon number at the position (x,y) after a t-step evolution.

In our experimental setup, the loss of photons is primarily attributed to losses incurred by various optical elements. Even in the case of a unitary quantum walk, the overall efficiency of our round-trip single-loop is approximately 0.71. The overall efficiency is derived by multiplying the transmission rates of each optical component employed in the round trip, which include the transmission rate of the beam splitter (~ 0.97), the efficiency of collecting photons from free space to fiber (~ 0.80), and the transmission rates of all other optical components (~ 0.91). Thus, we have $0.71 \simeq 0.97 \times 0.80 \times 0.91$. Besides, the measurement duration for a specific time step is approximately one hour, limited by the stability of our experimental setup.

Supplementary Note 4 - Initial state preparation and reconstruction of the center-of-mass motion

As discussed in the main manuscript, the initial excitation of the system should correspond to an equally-weighted superposition of Bloch eigenstates in a given lattice band. In our experiment, we cannot directly encode such an initial state since it contains excitation of both odd and even lattice sites, which is unfeasible with our setup. To overcome such a limitation, it is important to note that at each step, wave packets characterized by odd or even positions in the initial state do not interfere during the evolution process. This occurs because the evolved state exclusively occupy either even or odd positions when progressing to step t. We can take advantage of such a major property to split our experiment in two steps, where the initial excitation occupies either the even or odd lattice sites, and then reconstructing the wave packet dynamics exploiting the linearity of the system. To illustrate our strategy, let us consider the two-dimensional quantum walk as an example. We divided the experiment into two distinct parts, and we rewrite the initial state as

$$|\psi(0)\rangle=\left|\psi^1(0)\right\rangle+e^{\gamma_x-\gamma_y}\left|\psi^2(0)\right\rangle, \tag{29}$$

where

$$\left|\psi^1(0)\right\rangle=|1\rangle\otimes|0,0\rangle, \left|\psi^2(0)\right\rangle=|0\rangle\otimes|-1,1\rangle.$$

The evolved state is then $|\psi(t)\rangle=U^t|\psi(0)\rangle=U^t\left|\psi^1(0)\right\rangle+e^{\gamma_x t-\gamma_y t}U^t\left|\psi^2(0)\right\rangle$. Thus, the wave packet center of mass is given by

$$x_{CM}(t)=\frac{\sum_{x,y}\left[x\left|\langle\psi^1(x,y,t)|\psi^1(x,y,t)\rangle\right|+e^{2t(\gamma_x-\gamma_y)}x\left|\langle\psi^2(x,y,t)|\psi^2(x,y,t)\rangle\right|\right]}{\sum_{x,y}\left[|\langle\psi^1(x,y,t)|\psi^1(x,y,t)\rangle|+e^{2t(\gamma_x-\gamma_y)}|\langle\psi^2(x,y,t)|\psi^2(x,y,t)\rangle|\right]} \tag{30}$$

and

$$y_{CM}(t)=\frac{\sum_{x,y}\left[y\left|\langle\psi^1(x,y,t)|\psi^1(x,y,t)\rangle\right|+e^{2t(\gamma_x-\gamma_y)}y\left|\langle\psi^2(x,y,t)|\psi^2(x,y,t)\rangle\right|\right]}{\sum_{x,y}\left[|\langle\psi^1(x,y,t)|\psi^1(x,y,t)\rangle|+e^{2t(\gamma_x-\gamma_y)}|\langle\psi^2(x,y,t)|\psi^2(x,y,t)\rangle|\right]}. \tag{31}$$

One-dimensional quantum walks can also be realized with our setup by simply removing the free-space Mach-Zehnder interferometer. The probability distribution is obtained

$$P(x,t)=\frac{|\langle\psi(x,t)|\psi(x,t)\rangle|}{\sum_x|\langle\psi(x,t)|\psi(x,t)\rangle|}=\frac{N(x,t)}{\sum_x N(x,t)}, \tag{32}$$

where $N(x,t)$ is the total photon number at the position x after a t-step evolution.

Similarly, the chosen initial state can be written as

$$|\psi(0)\rangle=e^{\gamma_x}\left|\psi^1(0)\right\rangle+\left|\psi^2(0)\right\rangle, \tag{33}$$

where

$$\left|\psi^1(0)\right\rangle=|1\rangle\otimes|-1\rangle, \left|\psi^2(0)\right\rangle=|0\rangle\otimes|0\rangle. \tag{34}$$

The center of mass of the normalized involved state is

$$n_{CM}(t) = \frac{\sum_x \left(e^{2t\gamma_x} x \left|\langle\psi^1(x,t)|\psi^1(x,t)\rangle\right| + x \left|\langle\psi^2(x,t)|\psi^2(x,t)\rangle\right|\right)}{\sum_x \left(e^{2t\gamma_x} \left|\langle\psi^1(x,t)|\psi^1(x,t)\rangle\right| + \left|\langle\psi^2(x,t)|\psi^2(x,t)\rangle\right|\right)}. \tag{35}$$

Therefore, we perform two individual evolutions with different initial states, which finally enable us to reconstruct $x_{CM}(t)$, $y_{CM}(t)$, and $n_{CM}(t)$.

[1] Brunelli, M. *et al.* Restoration of the non-Hermitian bulk-boundary correspondence via topological amplification, *SciPost Phys.* **15**, 173 (2023).
[2] Longhi, S. Non-Hermitian skin effect and self-acceleration. *Phys. Rev. B* **105**, 245143 (2022).
[3] Heiss, W. D. The physics of exceptional points. *J. Phys. A* **45**, 444016 (2012).
[4] Longhi, S. Floquet exceptional points and chirality in non-Hermitian Hamiltonians, *J. Phys. A: Math. Theor.* **50**, 505201 (2017).
[5] Miri, M.-A. *et al.*, Exceptional points in optics and photonics. *Science* **363**, eaar7709 (2019).
[6] Longhi, S. *et al.*, Complex Berry phase and imperfect non-Hermitian phase transitions. *Phys. Rev. B* **107**, 085122 (2023).